Applied Physics A (2018) 124:439
https://doi.org/10.1007/s00339-018-1849-1

Applied Physics A
Materials Science & Processing

Sr- and Nb-co-doped $Li_7La_3Zr_2O_{12}$ solid electrolyte with Al_2O_3 addition towards high ionic conductivity

Changwei Lin[1] · Yu Tang[1] · Jun Song[1] · Lei Han[1] · Jingbo Yu[1] · Anxian Lu[1]

Received: 19 March 2018 / Accepted: 9 May 2018 / Published online: 21 May 2018

Abstract
In the present study, series of garnet-type $Li_{6.75+x}La_{3-x}Sr_xZr_{1.75}Nb_{0.25}O_{12}$ solid electrolytes [LLSZN with various Sr contents ($x = 0.05$–0.25)] have been prepared via conventional solid-state method. The effects of Sr contents on their phase structure and ionic conductivity have been systematically investigated on the combined measurements of X-ray diffraction and scanning electron microscopy and alter current impedance spectroscopy. Our results reveal that a phase transition from tetragonal to cubic structure occurs when both Sr and Nb elements is introduced, and such a cubic structure can be stable over the whole Sr contents variation, which is suggested to provide a beneficial impact on the performance of LLSZN. Accordingly, both relative density and total ionic conductivity exhibit a favorable tendency of increasing first and then decreasing with increased Sr contents, wherein a peak value at 93.46% and 5.09×10^{-4} S cm^{-1}, respectively, can be well achieved. Particularly, the maximum ionic conductivity is almost twice that of the compared sample (2.93×10^{-4} S cm^{-1}), and possess the minimum activation energy ~ 0.30 eV. Such a modification method, featured with higher efficiency and lower cost, is expected to be helpful for the development of solid electrolyte.

Keywords $Li_7La_3Zr_2O_{12}$ · Solid electrolyte · Li-ion conductivity · Solid-state reaction.

1 Introduction

Some issues involving low safety, stability, and poor cycling performances have occurred in traditional lithium ion (Li^+) batteries due to the presence of liquid electrolytes [1–3]. The presence of solid-state Li batteries (SSLiBs) makes it possible for solving suchlike questions, because solid rather than liquid electrolytes are employed in this case. Furthermore, SSLiBs have been found to possess high theoretical Li capacity and low negative potential [4–7], driving more searches on the design and exploitation of newly solid electrolyte materials. To date, a series of solid electrolytes involving perovskite-type titanate [8], NASICON-type phosphates [9, 10], and LISICON-type sulfides [11, 12] have been developed. Among these electrolytes, a class of garnet-type $Li_7La_3Zr_2O_{12}$ (LLZO) material attracts considerable attention by virtue of high ionic conductivity and wide electrochemistry potential window [13–15]. In fact, two kinds of phase structures including tetragonal and cubic phase occur in LLZO [13, 16–18]. The former of which features with an ordered structure that requires lithium located at the tetragonal 8a site and octahedral 16f and 32 g sites (space group I41/acd; No. 142) [16]. While the latter in LLZO crystal is a disordered structure with lithium at tetrahedral 24d Li(1) and octahedral 96 h Li(2) sites (space group Ia`3d; No. 230) [17]. Such a distinctly different arrangement for Li^+ would apply significant influence on the Li^+ conductivity; for instance, cubic LLZO exhibits intrinsically higher conductivity (two orders of magnitude higher) as compared with tetragonal-LLZO [13, 16]. In this sense, the cubic phase structure is a desirable for the improvement of conductivity. Unfortunately, such a structure is unable in nature. Therefore, efforts to incorporate structural stabilization technology are necessary for achieving higher performance LLZO electrolyte.

Recently, great progress in this aspect has been made by introducing doping modification. In particular, most studies

Electronic supplementary material The online version of this article (https://doi.org/10.1007/s00339-018-1849-1) contains supplementary material, which is available to authorized users.

✉ Anxian Lu
axlu@mail.csu.edu.cn

[1] School of Materials science and Engineering, Central South University, Changsha 410083, China

suggest that Al_2O_3 is a high-efficiency dopant in LLZO crystal helping to stabilize cubic phase, better yet, it can also serves as a solubilizer to decrease the sintering temperature approaching 230 °C [18–21]. For example, Geiger et al. [18] suggested that Al substitute for Li ($Al^{3+} \rightarrow 3Li^+$) might act to stabilize the cubic phase relative to the tetragonal phase. Furthermore, Rangasamy et al. [21] considered that Al^{3+} substituted for three Li^+ and two vacancies were formed according to the charge neutrality and was the vacancies concentration to determine the phase stability. Therefore, adding a certain amount of Al_2O_3 into LLZO is expected to facilitate the formation of cubic phase; simultaneously, drastical reduction in sintering temperature can be achieved. In addition, the incorporation of aliovalent element (i.e., Al, Nb, Ta, Te, Si, In, and Ge) into LLZO (aliovalent doping) has also been reported to stabilize the cubic phase of LLZO garnet with high Li^+ conductivity [19, 22–25].

As mentioned above, searching for suitable dopants has become a vital topic in the stabilization of cubic LLZO and the improvement of Li^+ conduction properties. In this direction, attempts to obtain LLZO solid solution substituted by either Ta^{5+} or Nb^{5+} have been found [26, 27]. In particular, the replacement of Nb^{5+} for Zr^{4+} in LLZO lattice with a nominal composition of $Li_{6.75}La_3Zr_{1.75}Nb_{0.25}O_{12}$ has maximized Li^+ conductivity up to 8×10^{-4} S·cm^{-1} [26], which is the maximum value reported to date (to our knowledge). In addition to doping effect, the microstructure associated with grain boundaries is another critical factor affecting the LLZO's quality and thus their practical application as a solid electrolyte or membrane electrode assembly in both all-solid-state lithium and lithium–air batteries. To be specific, a dense microstructure tends to promote the enhancement of total Li^+ conductivity (grain + grain boundaries) by reducing the grain-boundary resistance and restraining the dendritic growth during lithium deposition [28]. It is well established that sintering temperature can be reduced when the La^{3+} site in LLZO lattice is substituted by Sr^{2+} or Ce^{4+} [29, 30], while improved conductivity can be realized through substituting the other sites like Zr^{4+} by Nb^{5+} or Ta^{5+} [31, 32]. That is, the property enhancement for LLZO electrolytes strongly depends on the doping sites of aliovalent elements.

Hence, preparing a LLZO solid electrolyte with simultaneous replacement of La^{3+} and Zr^{4+} site is necessary for both practical production and applications. However, only a few data in this respect can be detected [28, 31, 32]. To accomplish it, double-doping technique seems as a feasible way, and the effects of their doping content variation on the phase structure, compactness, and Li^+ conduction behavior need further investigation. In the choice of material, Nb and Sr elements should stand out from aliovalent elements, because they are suggested to be an effective sintering and densification agents [33]. Besides, Sr ion (140 pm) exhibits a larger radius than La ion (130 pm), which is expected to play a positive role in the improvement of Li^+ conduction, since it has been found that the ion substitution with a larger diameter could widen the Li^+ migration pathway and thus increase the Li^+ mobility [34]. In addition, supervalent cation substitution can effectively increase the vacancy concentration and finally improve Li^+ conductivity by lowering the activation energy [35]. From the perspective of grain structures, high density, few boundaries, and good connectivity could help reduce intergranular impedance, and introducing sintering aids (like Al_2O_3) is a practical way to achieve it [28, 36, 37].

From the above, considering the complexity of co-doped system, we first design series $Li_{7-x}La_3Zr_{2-x}Nb_xO_{12}$ solid solution with various Nb contents, and confirm the optimal Nb doping contents ($x = 0.25$) for the highest Li^+ conductivity [26]. Based on this condition, we further synthesize Sr-doped $Li_7La_3Zr_{1.75}Nb_{0.25}O_{12}$ solid solution. For comparison, reference (pure $Li_{6.75}La_3Zr_{1.75}Nb_{0.25}O_{12}$) is prepared simultaneously. During sintering, 1.5 wt% Al_2O_3 was added into LLSZN to promote structure transition from tetragonal to cubic phase and decrease the sintering temperature [19, 38]. Subsequently, systematic investigations in terms of phase structure, relative density, and Li^+ conductivity have been carried out.

2 Experimental

2.1 Sample preparation

A conventional solid-state reaction procedure was employed for the preparation of $Li_{6.75+x}La_{3-x}Sr_xZr_{1.75}Nb_{0.25}O_{12}$ ($x = 0.05$–0.25), in which Li, La, Sr, Zr, and Nb sources come from high-purity Li_2CO_3 (Aladdin reagent, 99%), La_2O_3 (Sinopharm Chemical Reagent Co., Ltd, 99.99%), ZrO_2 (Sinopharm Chemical Reagent Co., Ltd, 99.9%), Nb_2O_5 (Sinopharm Chemical Reagent Co., Ltd., 99%), and $SrCO_3$ (Sinopharm Chemical Reagent Co., Ltd, 99.9%), respectively. $Li_{6.75}La_3Zr_{1.75}Nb_{0.25}O_{12}$ samples were also prepared for comparison. In particular, during sintering, an excess of 10 wt% Li_2CO_3, was added into the mixture to compensate the possible volatilization of Li. La_2O_3 was pre-dried at 900 °C for 10 h. Meanwhile, to lower the sintering temperature more effectively and further promote the formation and stabilization of cubic phase, 1.5 wt% Al_2O_3 (Sinopharm Chemical Reagent Co., Ltd, 99.5%) was also added. Subsequently, the mixtures were ball milled with zirconia balls in a 2-propanol solvent using Pulverisette 7 (Fritsch, Germany), wherein the milling time and rotate speed were set at about 10 h and 300 rpm, respectively. The mixtures were heated in 1000 °C for 10 h in an open alumina crucible and then cooled to room temperature. After that, the resultant powders were ground again using zirconia balls in 2-propanol solvent for 10 h. After evaporating mixture, the

powders were pressed into pellets (9.9 mm in diameter and 10 mm in thickness) by uniaxial pressure. Whereafter, a sintering process at 1150 °C for 15 h was performed on the pellets covered with mother powder to reduce possible Li loss.

2.2 Characterization

All element concentrations were determined by induced coupled plasma optical emission spectrometer (ICP-OES, VARIN VISTA-MPX). To investigate the effect of Sr contents on the phase structure, X-ray diffraction (XRD, D/max 2500 model, Japan) in $\theta - 2\theta$ configuration was carried out. A field-emission scanning electron microscope (SEM, Nova NanoSem 230) was employed to evaluate the surface morphology of sintered pellets, and the component distribution within them was characterized by the coupled energy dispersive X-ray spectroscopy (EDS). For the measurement of relative density, the Archimedes method was performed on the sintered pellets, during measurement, 2-propanol was using as the immersion medium. The ionic conductivity in $Li_{6.75+x}La_{3-x}Sr_xZr_{1.75}Nb_{0.25}O_{12}$ garnet material was measured by electrochemical workstation using a two-probe method. Before measurement, two sides of all samples were ground with SiC paper with 2000 grit. To prepare a complete electrode, Au, serving as Li-ion blocking electrodes, was sputtered on the top and bottom surfaces of the samples to form Au |LLSZN| Au specimen. Impedance spectra were collected from an electrochemical work station (ZAHNER-IM6ex) in the frequency region from 3×10^6 to 1 Hz.

3 Results and discussion

3.1 Structural characterization

Figure 1 shows the XRD patterns of $Li_{6.75+x}La_{3-x}Sr_xZr_{1.75}Nb_{0.25}O_{12}$ samples. The clear splitting peaks, shown in Fig. S1, are well presented in the un-doped sample (LLZO), indicating the existence of tetragonal phase, similar phenomenon can be found elsewhere [39]. The structure changes to a standard cubic structure when 0.25 mol Nb are introduced ($Li_{6.75}La_3Zr_{1.75}Nb_{0.25}O_{12}$ sample), according to the fact that the addition of Al_2O_3 during sintering could promote the formation of cubic phase [19, 38]. As for $Li_{6.75+x}La_{3-x}Sr_xZr_{1.75}Nb_{0.25}O_{12}$ sample (co-doped with Nb and Sr), nearly, pure cubic garnet structure can be identified, although a small amount of $La_2Zr_2O_7$ appear in the case of relative low Sr contents ($x = 0.05$ and 0.10), which may be ascribed to the loss of Li during the sintering process, although excess Li_2CO_3 has been added during preparation [40]. Notably, the diffraction peak intensity of $La_2Zr_2O_7$ becomes weaker as the x increases from 0.05 to 0.10. In addition, with Sr contents increasing to 0.15 or higher, the

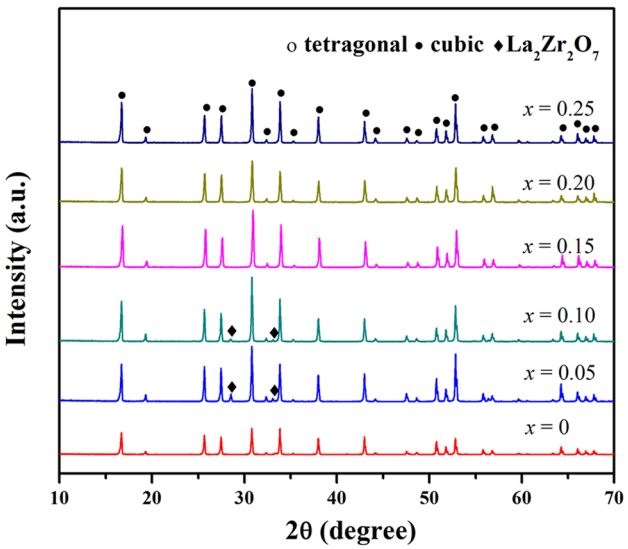

Fig. 1 XRD patterns of the $Li_{6.75+x}La_{3-x}Sr_xZr_{1.75}Nb_{0.25}O_{12}$ samples doped with different Sr contents (x)

signal from impurity phase disappears completely. That is, the samples co-doped with Nb and Sr exhibit a pure cubic structure. Considering no new phase related to Sr or Nb, the incorporation of both elements into LLZO would form a cubic LLZO solid solution structure, where part of La and Zr sites is substituted by additional Sr and Nb, respectively. In such a structure, the increased Sr contents would be followed by an increased Li, just as the stoichiometry of $Li_{6.75+x}La_{3-x}Sr_xZr_{1.75}Nb_{0.25}O_{12}$ shown, which, therefore, promotes the complete reaction of raw materials. Furthermore, the added Sr, as a solubilizer, could also decrease the sintering temperature and thus benefit to the formation of cubic phase to a certain degree [29, 33]. From the above, the LLSZN with a stable cubic structure can be prepared successfully via regulating the Sr contents.

Another interesting thing is the intensity of diffraction peak, as shown in Fig. S2, it can be seen that as the Sr contents increase, the intensity of the diffraction peak overall presents a trend of increasing first and then decreasing. According to the stoichiometric of $Li_{6.75+x}La_{3-x}Sr_xZr_{1.75}Nb_{0.25}O_{12}$, the contents of Sr and Li increase, while La contents decrease with increasing of x, when the sample free of Sr contents, the chemical formula of ceramic compositions is $Li_{6.75}La_3Zr_{1.75}Nb_{0.25}O_{12}$ and the ceramics is mainly composed of nearly pure cubic phase. It is found from Fig. 1 that the ceramics contain cubic LLZO phase, and a small amount of $La_2Zr_2O_7$ and the diffraction peak intensity of LLZO crystals increase with the increasing contents of Sr (x) and Li ($6.75 + x$) from 0.05 to 0.15, which means an increase in the LLZO contents. This phenomenon can be explained as follows: the increasing Li contents result in a reduction of sintering temperature, which makes

the diffusion of Li^+ and crystal growth of LLZO phase easy to occur. With further increasing Sr and Li contents, although diffusion of Li^+ is easier, due to La substituted by Sr severely, the obvious deviation of chemical composition ratio as compared to that of main crystal phase LLZO inevitable leads to the difficulties of LLZO crystals growth. As a result, a slight reduction in the LLZO crystal contents can be observed according to the change of diffraction peak intensity of LLZO crystals appearing on the XRD patterns.

The element contents for the samples are analyzed using ICP-OES and the results are summarized in Table 1, where the ratios are normalized with respect to the Nb contents. It is found that the measured molar ratio of Li/La/Nb approximately coincides with that of the formula unit $Li_{6.75+x}La_{3-x}Sr_xZr_{1.75}Nb_{0.25}O_{12}$ except Sr. The Sr contents by ICP-OES measurement was lower than stoichiometric ratio in LLSZN, possibly due to some uncertainty in the measurement of a small Sr contents with a low sample amount tested in ICP-OES (0.3 g). Sr from the raw material may also be partially vaporized during the high-temperature sintering [41]. However, Li evaporation becomes slighter with the increase of Sr contents. It can be easily seen from the ICP results that the evaporation of lithium is severer for the sample doped with Sr relative to Sr-free samples. This may probably as a result of Sr effect as a sintering agent.

3.2 Microstructure and elemental distribution

To investigate the role of Sr doping on the morphology of LLSZN samples, SEM measurement has been conducted on all samples. Before that, no treatment is done for ensuring the grain integrity. Without a doubt, this would directly cause more or less heterogeneous grains on sample surfaces, as shown in Fig. 2. Obviously, the samples with lower Sr contents ($x = 0.05$ and 0.10) exhibit relatively small grains with a diameter ranging from 20 to 60 μm, small amount of closed pores between grains can be clearly observed, indicating poor density. With Sr contents increasing to $x = 0.15$, good connection between grains without small pores is expected to reduce the grain-boundary resistance [28]. This is, increased Sr contents could densify the microstructure of LLSZN. It is worth mentioning that the denser structure

Table 1 Element composition of the pellets with different Sr contents sintered at 1150 °C for 15 h

x in $Li_{6.75+x}La_{3-x}Sr_xZr_{1.75}Nb_{0.25}O_{12}$		0	0.05	0.10	0.15	0.20	0.25
Li content (theoretical)		6.75	6.80	6.85	6.90	6.95	7.00
ICP results	Li	6.15	6.42	6.51	6.57	6.65	6.68
	La	3.0	2.99	3.01	3.02	3.00	3.02
	Sr	n.o	0.03	0.08	0.12	0.18	0.21
	Nb	0.25	0.25	0.25	0.25	0.25	0.25
	Al	0.25	0.25	0.25	0.25	0.26	0.25

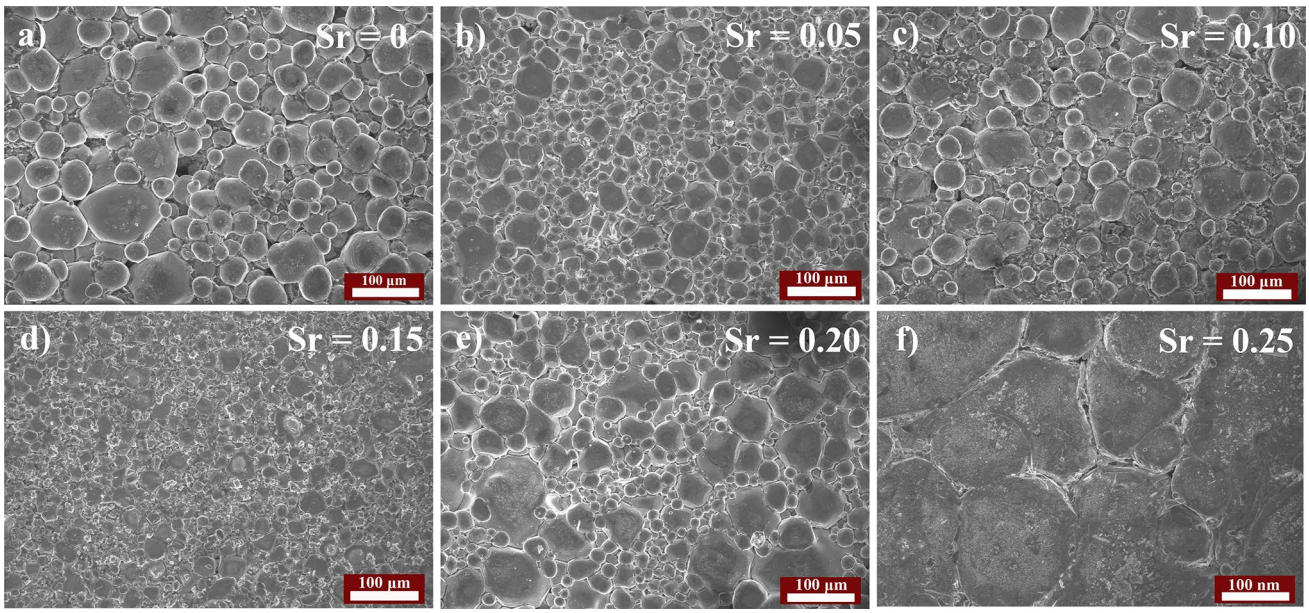

Fig. 2 SEM images for the $Li_{6.75+x}La_{3-x}Sr_xZr_{1.75}Nb_{0.25}O_{12}$ samples with different Sr contents (x)

allows the Li^+ easier to be transported [42]. However, this phenomenon is not permanent over the whole Sr contents, when it further increases to 0.20, the grain size gradually grows up to 100 μm, and, meanwhile, the grain boundaries start showing the fusion tendency. More evident image can be detected in the case of Sr contents of 0.25. Therefore, it is reasonable to draw a conclusion that the increased Sr into LLSZN sample could promote sintering; in particular, optimized Sr contents at 0.15 mol lead to excellent structure with a good connection between the grains and dense structure, which must play an important role in the electrical performances.

EDS measurement was carried out. As can be seen in Fig. 3, the Al element is mainly accumulated at the grain boundaries; instead of grain interior, similar phenomenon can be found in other reports [27]. However, opposite case occurs in the Sr and Nb elements, close observation of the figure demonstrates that the distribution of Sr in the mapping is basically the same as the distribution of La, as is the case of Nb and Zr, and a main accumulation of them inside grains can be observed, which accords with the fact that doped elements tend to enter garnet lattice and form solid solution structure.

3.3 Electrical property

The Nyquist plots of LLSZN pellets with different Sr contents measured at 25 °C are shown in Fig. 4. While the

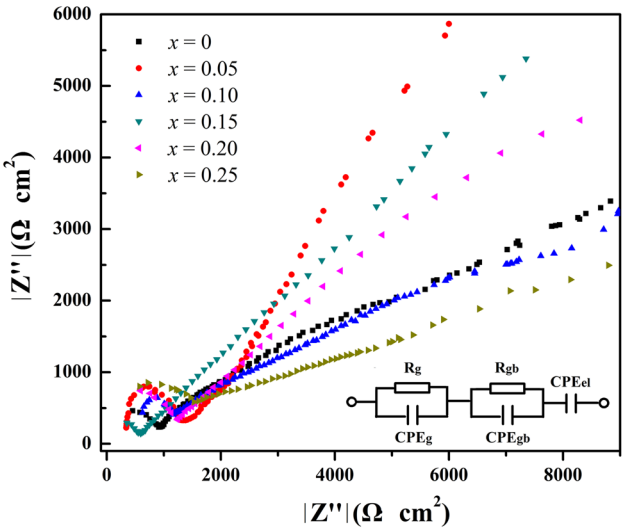

Fig. 4 Nyquist plots of $Li_{6.75+x}La_{3-x}Sr_xZr_{1.75}Nb_{0.25}O_{12}$ pellets with different Sr contents (x) measured at room temperature

Nyquist plot of un-doped sample is shown in Fig. S3. For all samples, the Nyquist plots are composed of one semicircle and a tail. Here, separate contributions from grains and grain boundaries cannot be well distinguished, since one semicircle instead of two has been obtained, and the grain-boundary semicircle might be overlapped by that of the grains. Generally speaking, the appearance of tail at low

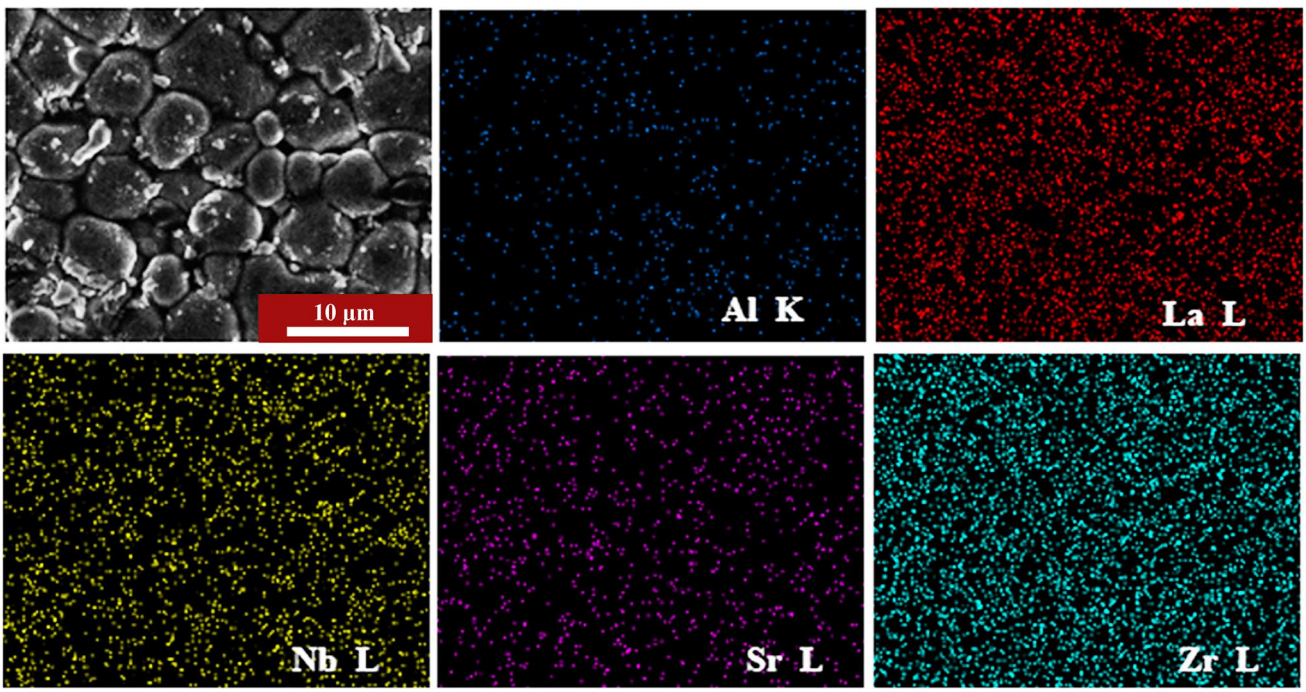

Fig. 3 SEM and EDS elemental mapping images showing elemental distribution in $Li_{6.9}La_{2.85}Sr_{0.15}Zr_{1.75}Nb_{0.25}O_{12}$

frequency belongs to Warburg-type impedance, corresponding to the diffusion of Li^+ in the gold-blocking electrodes. This is an indication for intrinsic ionically conduction of the investigated materials [24, 37]. Based on high-frequency intercept on the Z′-axis and the sample's dimension, the total (grain and grain boundary) ionic conductivity (σ_t) can be obtained. During data processing, an (R_gCPE_g)($R_{gb}CPE_{gb}$)(CPE_{el}) equivalent circuit can be applied to fit all the EIS using Zview software, where R is the resistance, CPE is the constant phase element, and the subscripts g, gb, and el refer to grain, grain boundary, and Au electrode, respectively. Total conductivity can be calculated by the following equation:

$$\sigma = \frac{l}{\mathrm{RS}} \tag{1}$$

in which R is resistance, l is sample thickness, and S denotes the area of the electrodes. The total conductivity of LLSZN ceramic samples can be obtained by fitting this equivalent circuit, as shown in Fig. 4. As listed in Table 2, the variation of σ_t with Sr contents (x) is presented. For the garnet family of ceramic materials, regardless of some of singular points, the general variation trend of σ_t with Sr contents (x) is increasing first and then decreasing. The calculated conductivity for the $Li_{6.75}La_3Zr_{1.75}Nb_{0.25}O_{12}$ sample (2.96×10^{-4} S cm^{-1}) in our work is slightly lower than the reported one (1200 °C 36 h) [26], much lower sintering temperature and shorter holding time dominant the difference. The maximum value at 5.09×10^{-4} S cm^{-1} can be achieved when $x=0.15$; notably, it is relatively high among the values obtained under such a condition (25 °C). As we all known, in the garnet family of ceramic electrolytes, in addition to the cubic phase, the high density provides indispensable contributions for the improvement of conductivity [42, 43].

For explaining such a high conductivity, the quantitative results in terms of relative density (RD) are measured and are summarized in Table 2. Obviously, RD exhibits a similar trendy with σ_t to increase first and drop subsequently when x increases from 0 to 0.25, and the highest relative density (~93.5%) occurs at the optimized Sr contents ($x=0.15$).

Table 2 Doping amount, total conductivity (σ_t) measured at 25 °C, activation energy (E_t), and relative density (RD) for $Li_{6.75+x}La_{3-x}Sr_xZr_{1.75}Nb_{0.25}O_{12}$ electrolytes prepared at 1150 °C for 15 h

x	σ_t ($\times10^{-4}$ S cm^{-1})	E_a (eV)	RD (%)
0	2.93 ± 0.13	0.325	90 ± 0.61
0.05	2.13 ± 0.21	0.35	90.57 ± 0.92
0.10	2.31 ± 0.28	0.346	91.15 ± 1.12
0.15	5.09 ± 0.38	0.30	93.46 ± 1.01
0.20	2.41 ± 0.14	0.34	91.92 ± 0.93
0.25	1.85 ± 0.15	0.357	88.99 ± 0.74

Such a high density should be attributed to the existence of $SrCO_3$ when Sr contents are added, which would serve as a sintering aid to facilitate densification. While the conductivity of un-doped sample is two orders of magnitude lower than Sr-doped samples and has higher activation energy (0.423 eV), shown in Table S1, this is due to tetragonal structure and lower relative density. To reveal the underlying relationship between density and conductivity, Fig. 5 plots the variation of density, total conductivity, and grain conductivity at different Sr contents. As can be seen in Fig. 5, all of the curves can be simply divided into two stages over the whole Sr contents. Namely, an initial increase to maximum value followed by a subsequent decrease to minimum value, i.e., a good linear relationship exists between the relative density and ionic conductivity of LLSZN; this is a common phenomenon [42, 43]. As mentioned above, the synergistic effects of Li loss during sintering (Table 1) and the formation of few impurities phase (Fig. 1) could impede the movement of Li^+, and finally lower the conductivity for the samples with lower Sr contents ($x=0.05$ and 0.10). The highest total conductivity and grain conductivity obtained at $x=0.15$ are related to the highest relative density (93.5%). However, much more Sr contents ($x>0.15$) bring the conductivity down, although there would be more Li contents (carriers) when introduced Sr contents increase according to the formula of $Li_{6.75+x}La_{3-x}Sr_xZr_{1.75}Nb_{0.25}O_{12}$. Such a strange behavior has been reported by Kihira et al. [31], and this is because in the doped LLZO solid electrolyte, an issue involving the balance of lithium occupancy between lithium sites (24 d and 96 h) should be taken into consideration, which is suggested to be more vital than the total number of lithium contents.

The temperature dependence of total conductivity for the LLSZN pellets with various Sr contents follows the Arrhenius behavior, as shown in Fig. 6. For the un-doped sample,

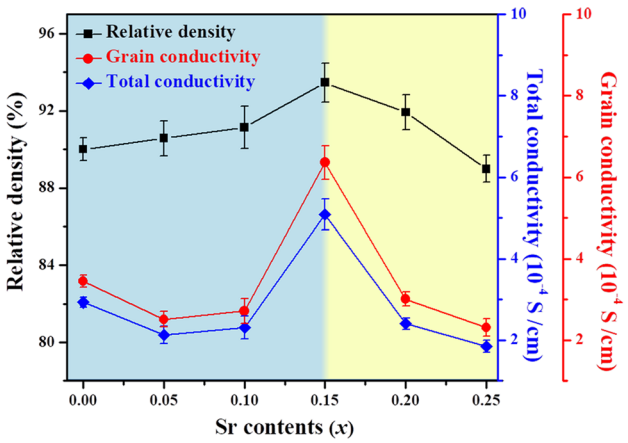

Fig. 5 Density, total conductivity, and grain conductivity of the $Li_{6.75+x}La_{3-x}Sr_xZr_{1.75}Nb_{0.25}O_{12}$ samples with different Sr contents (x)

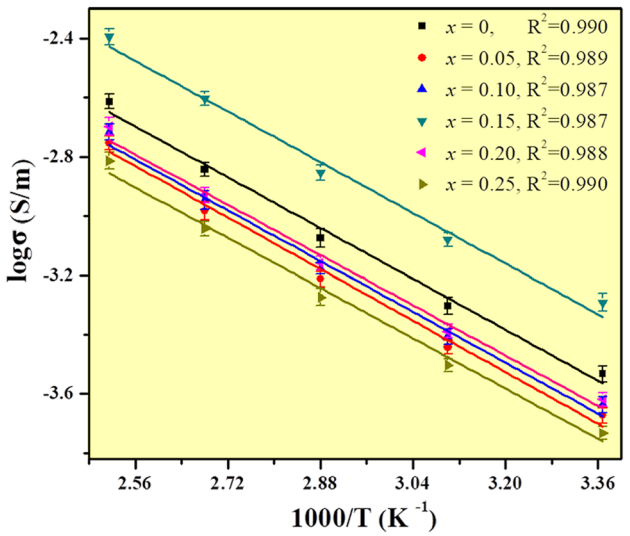

Fig. 6 Arrhenius plots of total conductivities of the $Li_{6.75+x}La_{3-x}Sr_xZr_{1.75}Nb_{0.25}O_{12}$ samples with different Sr contents (x)

the Arrhenius plot of total conductivity is shown in Fig. S4. Every sample was measured in the temperature range from 25 to 125 °C. From the results, the activation energies (E_a) of the total ionic conductivities within the observed temperature can be calculated by the following equation (2):

$$\sigma T = A\exp\left(\frac{-E_a}{k_B T}\right), \tag{2}$$

where A, k_B, and T are the pre-exponential parameter, Boltzmann's constant, and absolute temperature, respectively. Thus, the corresponding activation energies for each conductivity can be calculated as the slope of the logσ versus 1000/T (detail values see Table 2). Clearly, the conductivity values (logσ) exhibit well linear relation with the reciprocal of the temperature, meaning that all the Sr-doped LLSZN samples possess an identical ion conductive mechanism within such a temperature range. Here, the lowest activation energy value at 0.30 eV appears in the LLSZN with $x = 0.15$; the other samples show significantly increased E_a and all of them lower than 0.36 eV, while the activation energy of undoped sample up to 0.423 eV. By consulting relevant studies [44], three possible reasons may be responsible for the reduction of E_a: (1) the increased vacancies caused by adding higher valence element (Nb); (2) lower grain-boundary resistance derived from higher density; and (3) wider ionic diffusion pathway on the basis of introducing larger ionic diameter element (Sr^{2+}).

In a word, the simultaneous incorporation of Nb and Sr dopant into LLZO could further improve the ionic conductivity as compared with single-doped materials; moreover, the sintering time for the formation of cubic LLZO can be shortened. Furthermore, to show the superiority of the double-doped materials in this work, the latest literatures related to Li-ion conductivity can be found [28, 37, 44–49]. Table 3 clearly displays the comparison of the total conductivity (σ_{total}) between our result and other LLZO materials doped with various elements; their sintering condition and activation energies (E_a) are also given. Here, the ionic conductivity of $Li_{6.9}La_{2.85}Sr_{0.15}Zr_{1.75}Nb_{0.25}O_{12}$ at 5.09×10^{-4} S·cm^{-1} occupies the highest level, excepting that of $Li_7La_3ZrNb_{0.5}Y_{0.5}O_{12}$, much higher sintering temperature at 1230 °C may contribute to it. Overall, the performance of as-synthesized LLZO solid electrolyte co-doped with Sr and Nb performs better in the Li-ion conductivity, which is suitable for practical application.

4 Conclusions

In summary, high lithium conductivity $Li_{6.75+x}La_{3-x}Sr_xZr_{1.75}Nb_{0.25}O_{12}$ solid electrolyte with cubic structure has been prepared with the Al_2O_3 addition via solid-state reaction after sintering at 1150 °C for 15 h. In our work, we adopt double-element doping technology based on the constant Nb contents at 0.25 that guarantees high Li^+ conductivity, and optimal 1.5 wt% Al_2O_3, as sintering

Table 3 Literature overview of sintering condition, total conductivity (σ_{total}) at room temperature, and activation energies (E_a) in aliovalently doped LLZO

Compounds	Sintering condition	σ_{total} ($\times10^{-4}$ S·cm^{-1})	E_a (eV)	References
$Li_{6.23}Al_{0.26}La_3Zr_{1.88}O_{11.76}$	1150 °C for 6 h	2.54	–	[45]
$Li_7La_3Zr_2O_{12}$-$Al_{0.1}$	1150 °C for 15 h	1.41	0.31	[46]
$Li_7La_3Zr_{1.7}Ti_{0.3}O_{12}$	1180 °C for 20 h	4.16	0.48	[37]
$Li_{6.45}Ca_{0.05}La_{2.95}Ta_{0.6}Zr_{1.4}O_{12}$	1125 °C for 6 h	2.84	–	[49]
$Li_{5.25}La_3Ta_{1.75}Ge_{0.25}O_{12}$	1100 °C for 10 min	0.840	–	[47]
$Li_{6.775}Al_{0.05}La_3Zr_{1.925}Sb_{0.075}O_{12}$	1170 °C for 6 h	4.10	0.32	[48]
$Li_{6.6}La_{2.75}Y_{0.25}Zr_{1.6}Ta_{0.4}O_{12}$	1200 °C for 18 h	4.36	0.34	[28]
$Li_7La_3ZrNb_{0.5}Y_{0.5}O_{12}$	1230 °C for 15 h	6.53	0.306	[44]
$Li_{6.9}La_{2.85}Sr_{0.15}Zr_{1.75}Nb_{0.25}O_{12}$	1150 °C for 15 h	5.09	0.30	This work

agent, was added to promote the cubic structure formation in low sintering temperature; our results highlight the effect of Sr element on the phase structure and Li^+ conductivity. It is found that the Sr addition effectively promotes ceramic sintering and the formation of dense microstructure. Structurally, both Sr and Nb atoms enter the garnet lattice to form solid solution structure, which improves the electrical properties. To be special, the maximum relative density and ionic conductivity follows Sr contents to increase first and then decrease a peak value at 93.46% and 5.09×10^{-4} S cm^{-1}, respectively, can be well achieved at 0.15 molar Sr and possess the lowest activation energy of 0.30 eV. The present study indicates the possibility of enhancement in the density and total Li^+ conductivity of LLSZN through a suitable and optimal dopant contents. Therefore, Stoichiometric formula in $Li_{6.9}La_{2.85}Sr_{0.15}Zr_{1.75}Nb_{0.25}O_{12}$ with 1.5 wt% Al_2O_3 may be a promising solid-state ceramic electrolyte for all-solid-state lithium rechargeable batteries.

Acknowledgements This work has been supported by the project of Technology Promotion and Industrialization for key basic Materials in China (No. 2017YFB0310200) and the National Nature Science Foundation of China (No. 51672310, 51272288, 51172286).

References

1. J.C. Bachman, S. Muy, A. Grimaud, H.H. Chang, N. Pour, S.F. Lux, O. Paschos, F. Maglia, S. Lupart, P. Lamp, L. Giordano, Y. Shao-Horn, Chem. Rev. **116**, 140–162 (2016)
2. Y. Kato, S. Hori, T. Saito, K. Suzuki, M. Hirayama, A. Mitsui, M. Yonemura, H. Iba, R. Kanno, Nat. Energy **1**, 16030 (2016)
3. K. Takada, Acta Mater. **61**, 759–770 (2013)
4. H. Zhang, C. Li, M. Piszcz, E. Coya, T. Rojo, L.M. Rodriguez-Martinez, M. Armand, Z. Zhou, Chem. Soc. Rev. **46**, 797–815 (2017)
5. Y. Liu, D. Lin, P.Y. Yuen, K. Liu, J. Xie, R.H. Dauskardt, Y. Cui, Adv. Mater. **29**, 1605531 (2017)
6. V. Thangadurai, S. Narayanan, D. Pinzaru, Chem. Soc. Rev. **43**, 4714–4727 (2014)
7. C.K. Chan, T. Yang, J.Mark Weller, Electrochim. Acta **253**, 268–280 (2017)
8. J.W. Fergus, J. Power Sources **195**, 4554–4569 (2010)
9. N. Kamaya, K. Homma, Y. Yamakawa, M. Hirayama, R. Kanno, M. Yonemura, T. Kamiyama, Y. Kato, S. Hama, K. Kawamoto, A. Mitsui, Nat. Mater. **10**, 682–686 (2011)
10. K. Arbi, J.M. Rojo, J. Sanz, J. Eur. Ceram. Soc. **27**, 4215–4218 (2007)
11. K. Aso, A. Sakuda, A. Hayashi, M. Tatsumisago, ACS Appl. Mater. Interfaces **5**, 686–690 (2013)
12. J. Haruyama, K. Sodeyama, L. Han, K. Takada, Y. Tateyama, Chem. Mater. **26**, 4248–4255 (2014)
13. R. Murugan, V. Thangadurai, W. Weppner, Angew. Chem. **46**, 7778–7781 (2007)
14. M. Kotobuki, H. Munakata, K. Kanamura, Y. Sato, T. Yoshida, J. Electrochem. Soc. **157**, A1076 (2010)
15. K. Kajihara, N. Tezuka, M. Shoji, J. Wakasugi, H. Munakata, K. Kanamura, B. Chem. Soc. Jpn. **90**, 1279–1286 (2017)
16. J. Awaka, N. Kijima, H. Hayakawa, J. Akimoto, J. Solid State Chem. **182**, 2046–2052 (2009)
17. J. Awaka, A. Takashima, K. Kataoka, N. Kijima, Y. Idemoto, J. Akimoto, Chem. Lett. **40**, 60–62 (2011)
18. C.A. Geiger, E. Alekseev, B. Lazic, M. Fisch, T. Armbruster, R. Langner, M. Fechtelkord, N. Kim, T. Pettke, W. Weppner, Inorg. Chem. **50**, 1089–1097 (2011)
19. M. Kotobuki, K. Kanamura, Y. Sato, T. Yoshida, J. Power Sources **196**, 7750–7754 (2011)
20. A. Düvel, A. Kuhn, L. Robben, M. Wilkening, P. Heitjans, J. Phys. Chem. **116**, 15192–15202 (2012)
21. E. Rangasamy, J. Wolfenstine, Sakamoto, Solid State Ionics **206**, 28–32 (2012)
22. H. Imagawa, S. Ohta, Y. Kihira, T. Asaoka, Solid State Ionics **262**, 609–612 (2014)
23. Y. Wang, W. Lai, Electrochem. Solid State Lett. **15**, 68 (2012)
24. C. Deviannapoorani, L. Dhivya, S. Ramakumar, R. Murugan, J. Power Sources **240**, 18–25 (2013)
25. M. Huang, A. Dumon, C.W. Nan, Electrochem. Commun. **21**, 62–64 (2012)
26. S. Ohta, T. Kobayashi, T. Asaoka, J. Power Sources **196**, 3342–3345 (2011)
27. Y. Li, J.T. Han, C.A. Wang, H. Xie, J.B. Goodenough, J. Mater. Chem. **22**, 15357 (2012)
28. L. Dhivya, R. Murugan, ACS Appl Mater. Interfaces **6**, 17606–17615 (2014)
29. A. Dumon, M. Huang, Y. Shen, C.W. Nan, Solid State Ionics **243**, 36–41 (2013)
30. E. Rangasamy, J. Wolfenstine, J. Allen, J. Sakamoto, J. Power Sources **230**, 261–266 (2013)
31. Y. Kihira, S. Ohta, H. Imagawa, T. Asaoka, ECS Electrochem. Lett. **2**, 56–59 (2013)
32. L.J. Miara, S.P. Ong, Y. Mo, W.D. Richards, Y. Park, J.M. Lee, H.S. Lee, G. Ceder, Chem. Mater. **25**, 3048–3055 (2013)
33. B.S.M.J. Roy, Ionics **18**, 291–297 (2011)
34. W. Bucheli, T. Duran, R. Jimenez, J. Sanz, A. Varez, Inorg. chem. **51**, 5831–5838 (2012)
35. M.M. Ahmad, RSC Adv. **5**, 25824–25829 (2015)
36. R. Murugan, S. Ramakumar, N. Janani, Electrochem. Commun. **13**, 1373–1375 (2011)
37. C. Shao, Z. Yu, H. Liu, Z. Zheng, N. Sun, C. Diao, Electrochim. Acta **225**, 345–349 (2017)
38. Y.H. Zhang, F. Chen, R. Tu, Q. Shen, L.M. Zhang, Key Eng. Mater. **616**, 217–222 (2014)
39. R. Takano, K. Tadanaga, A. Hayashi, M. Tatsumisago, Solid State Ionics **255**, 104–107 (2014)
40. M. Huang, T. Liu, Y. Deng, H. Geng, Y. Shen, Y. Lin, C.W. Nan, Solid State Ionics **204**, 41–45 (2011)
41. Y. Zhang, D.E. Mack, M.O. Jarligo, X. Cao, R. Vaßen, D. Stöver, J. Therm. Spray Technol. **18**, 694–701 (2009)
42. J.L. Allen, J. Wolfenstine, E. Rangasamy, J. Sakamoto, J. Power Sources **206**, 315–319 (2012)
43. Y. Kim, H. Jo, J.L. Allen, H. Choe, J. Wolfenstine, J. Sakamoto, G. Pharr, J. Am. Ceram. Soc. **99**, 1367–1374 (2016)
44. J. Gai, E. Zhao, F. Ma, D. Sun, X. Ma, Y. Jin, Q. Wu, Y. Cui, J. Eur. Ceram. Soc. **38**, 1673–1678 (2018)
45. X.X. Pan, J.X. Wang, X.H. Chang, Y.D. Li, W.B. Guan, Solid State Ionics **317**, 1–6 (2018)
46. P. Zhao, G. Cao, Z. Jin, H. Ming, Y. Wen, Y. Xu, X. Zhu, Y. Xiang, S. Zhang, Mater. Design **139**, 65–71 (2018)
47. M. Kotobuki, S. Song, R. Takahashi, S. Yanagiya, L. Lu, J. Power Sources **349**, 105–110 (2017)
48. T. Yang, Y. Li, W. Wu, Z. Cao, W. He, Y. Gao, J. Liu, G. Li, Ceram. Int. **44**, 1538–1544 (2018)
49. X. Chen, T. Cao, M. Xue, H. Lv, B. Li, C. Zhang, Solid State Ionics **314**, 92–97 (2018)